HHS Public Access

Author manuscript

Electroanalysis. Author manuscript; available in PMC 2023 August 03.

Published in final edited form as:

Electroanalysis. 2022 December ; 34(12): 1961–1975. doi:10.1002/elan.202200091.

In-plane Extended Nano-coulter Counter (XnCC) for the Label-free Electrical Detection of Biological Particles

Zheng Zhao[a,b], **Swarnagowri Vaidyanathan**[a,b], **Payel Bhanja**[c,d], **Sachindra Gamage**[b,e], **Subhrajit Saha**[c,d], **Collin McKinney**[b,f], **Junseo Choi**[b,f], **Sunggook Park**[b,f], **Thilanga Pahattuge**[b,e], **Harshani Wijerathne**[b,e], **Joshua M. Jackson**[b,e], **Mateusz L. Huppert**[g], **Małgorzata A. Witek**[b,e], **Steven A. Soper**[a,b,d,e,h,i]

[a]Bioengineering Program, The University of Kansas, Lawrence, KS 66045

[b]Center of BioModular Multiscale Systems for Precision Medicine, The University of Kansas, Lawrence, KS 66045

[c]Department of Radiation Oncology, University of Kansas Medical Center, Kansas City, KS 66160

[d]University of Kansas Cancer Center, University of Kansas Medical Center, Kansas City, KS 66160

[e]Department of Chemistry, The University of Kansas, Lawrence, KS 66045

[f]CRITCL, The University of North Carolina, Chapel Hill, NC

[g]Department of Industrial and Mechanical Engineering, Louisiana State University, Baton Rouge, LA 70803

[h]BioFluidica, Inc., San Diego, CA

[i]Department of Mechanical Engineering, The University of Kansas, Lawrence, KS 66045

Abstract

We report an in-plane extended nanopore Coulter counter (XnCC) chip fabricated in a thermoplastic via imprinting. The fabrication of the sensor utilized both photolithography and focused ion beam milling to make the microfluidic network and the in-plane pore sensor, respectively, in Si from which UV resin stamps were generated followed by thermal imprinting to produce the final device in the appropriate plastic (cyclic olefin polymer, COP). As an example of the utility of this in-plane extended nanopore sensor, we enumerated SARS-CoV-2 viral particles

ssoper@ku.edu .

Credit Author Statement

ZZ – performed the majority of the XnCC characterization work, worked on the application demonstrations, and wrote some of the manuscript; SV –produced the simulation results and assisted in the XnCC fabrication and metrology; PB – assisted in radiation exposure of mouse models; SS – generated the concept of EVs for radiation exposure and supplied mouse models for these studies; CM – assisted with the electrical analysis of the XnCC; JC and SP – performed the FIB milling of the nanostructures into the SI wafer for XnCC chip development; TP – performed the selectin and release of the VPs; HW – assisted in the review of this manuscript and composed TOC graphic; JMJ – generated figure 1 and helped to write manuscript; MLH – provided the pillared affinity chips for this work; MAW – produced the VP/EV selection chips with the surfaces decorated with the affinity agents and assisted in VP/EV selection and release; SAS – secured project funding, guided and consulted with the experimentation, and reviewed and the manuscript.

(VPs) affinity-selected from saliva and extracellular vesicles (EVs) affinity-selected from plasma samples secured from mouse models exposed to different ionizing radiation doses.

Keywords

Coulter counter; nanoparticles; COVID-19; exosomes

1 Introduction

Coulter counters can provide label-free detection of particles based on resistive-pulse sensing (RPS) to determine the size, concentration, surface charge, and permeability of the relevant particles [1–5]. RPS requires the use of a narrow constriction in series with a larger fluidic network that flank each side of the constriction with a voltage applied across the fluidic network. RPS measures either a change in current or potential when a particle is resident within the pore due to a portion of the carrier electrolyte being displaced by the relevant particle creating a change in the resistivity across the electrically biased pore [6].

$$\Delta E = \frac{Ed^3\left[1-0.8(d/D)^3\right]^{-1}}{LD^2(1+4\rho/D\rho_s)(1+\alpha)} \rightarrow \Delta E = \frac{d^3}{\left[1-0.8(d/D)^3\right]} \cdot Constant \quad (1)$$

The change in voltage arising from resistance changes when a particle occupies the pore can be described using equation 1, where ΔE is the voltage change between the occupied and unoccupied pore, E is the applied potential, ρ_S is the pore surface resistivity, α is the pore-to-load resistance, L is the effective length of the nanopore, d is the particle diameter, D is the pore diameter, and ρ is the fluid resistivity [5,7]. For most RPS cases, the majority of the parameters shown in equation 1 remain constant during a measurement when a rigid pore and homogeneous electrolyte are used and the only variable that changes is the particle diameter; the size profile of the particles in the sample can be deduced by analyzing the amplitude of RPS events. In addition, with a known flow rate the concentration of the particles in the sample can be obtained. An important note with respect to equation 1 is that the measured signal, ΔE, will depend on the ratio d^3/D^2 and as such for measurable signals, the pore diameter needs to be close to the particle diameter (for this work, particles measured were <200 nm in size).

Equation 1 is applicable to non-conductive particles because additional parameters must be considered for conductive particles, including surface charge, particle charge density, and permeability.[1,5] For permeable particles, the particle resistivity may be lower than the carrier electrolyte due to the internal composition of the particle. As a result, different particles can produce different signal polarities when measured in a similar electrolyte [1,8,9].

RPS detectors can be configured in one of two formats: (i) Out-of-plane sensors in which the pore is situated within a high resistance membrane that separates two electrolyte reservoirs filled with a conducting medium; and (ii) in-plane sensors in which the pore is placed in the same plane as the accompanying fluidic network. Using either format, RPS has been demonstrated for the analysis of viruses [10–13], bacteria [14, 15], Au nanoparticles [16, 17], cells [18–20], proteins [21, 22], and DNA [23, 24]. RPS has also been combined with microfluidic technology [12]. For example, Sohn and team have developed a PDMS-based in-plane RPS to measure single DNA molecules [25], and multiple stage photolithography and electron beam lithography with dry etching for pattern transfer into a quartz substrate [26]. In the PDMS example, the SU-8 master was made using a combination of photolithography (microstructures) and electron-beam lithography (nanostructures) from which replicas could be generated using soft lithography. A similar PDMS device was reported by Fraikin *el al.* [12] for nanoparticle counting at high speeds, which has been commercialized by Spectradyne (https://nanoparticleanalyzer.com/). As another example of the use of in-plane pores, Jacobson and team have used these sensing devices for characterizing hepatitis B virus capsids and monitoring virus capsid assembly [27, 28]. In these sensors, the devices were made by direct focused ion beam milling into inorganic substrates, such as glass, Si, or quartz.

We report an in-plane extended nano-Coulter counter (XnCC) device for analyzing biological particles, including virus particles (VPs) and extracellular vesicles (EVs), for measuring the size and concentration of the particles using a device fabricated in a thermoplastic with the target particles affinity-selected from complex biological samples. When a particle travels through the in-plane pore sensor, a transient signal is recorded (Figures 1a–b). The in-plane pore used herein was designed with a size of 200×200×100 nm (W×H×L; extended nanofluidics [29]) and fabricated by imprinting into a thermoplastic; in this manuscript cyclic olefin polymer, COP, was used as the plastic for the XnCC. The XnCC chip showed the capability to sense EVs or VPs<200 nm in size with an amplifier to record the current signal trace to determine peak amplitude and width. A potential was clamped across the in-plane pore, and the resistance of the electrolyte in the device was considered as a series connection in the circuit (Figure 1c). Whenever a VP/EV traveled through the in-plane pore sensor, the intra-particle content formed a parallel circuit with the pore. Figure 1c shows the equivalent sensing circuit for the XnCC chip, where R_{mc} is the resistance of the microchannel, R_{nc} is the resistance of the nanochannel, R_{np} is the resistance of the in-plane nanopore sensor, and R_p is the resistance of the particle. In Figure 1d, expressions for the current flow in the circuit are given for the open pore and occupied conditions, with the net signal measured (ΔI) given as the difference between the open and occupied in-plane pore sensor currents. Using equation (1), we show in Figure 1e the particle blockage current (ΔI) as a function of particle size with respect to the in-plane pore size. As can be seen from Figure 1e, for a 20 pA threshold, which is determined by the noise in the open pore current measurements, we should be able to detect a particle size of 60 nm (diameter); the data presented in this manuscript will demonstrate our ability to measure 46 nm particles with the aforementioned in-plane pore sensor.

Compared to other technologies, our XnCC chip has several advantages: (1) The pre-selection of target particles in a small volume (~ 30 μL) using a microfluidic chip prior

to counting; (2) high-resolution electronic signal recordings to provide reliable and accurate information in terms of particle size (peak amplitude) and particle travel time (peak width) as well as particle concentration; (3) dynamic range of 10^5 to 10^9 particles/mL with a 100,000 Hz sampling frequency and 10 KHz bandwidth; and (4) the device made in a thermoplastic to allow for high-scale production at low cost using, for example, injection molding [30]. The production rate and cost per unit for a thermoplastic injection molded is lower than PDMS-based devices (> 1,000 units per machine per day at ~ $2 per unit).

Because RPS can detect any particle with a size commensurate with the pore size (d^3/D^2 dependence as shown in equation (1)), it becomes necessary when analyzing complex samples containing a heterogeneous mixture of particles to pre-select the target(s) with high specificity. In this case, affinity selection can be used to target the required particle population for analysis to add specificity to the assay. By targeting specific proteins on the surface of particles, such as VPs and EVs using affinity agents (aptamer or antibodies), a specific type of particle can be collected and then enumerated using RPS. Affinity agents can be immobilized onto a substrate, such as the surface of a microplate, beads, or even microfluidic devices, to allow for the solid phase selection of targets that can subsequently be released for analysis (*i. e.*, catch and release) [31]. Using affinity selection, the isolation can result in high specificity and purity [32–34]. For example, we reported a microfluidic device made from a plastic via micro-injection molding that could affinity select EVs from plasma samples and release them [35]. This report used anti-CD8 antibodies to select EVs using a microfluidic with their mRNA cargo used to diagnose acute ischemic stroke.

2 Experimental

2.1 XnCC Chip Fabrication

An XnCC master mold was made from a Cr coated silicon (Si) wafer with the XnCC chip containing both micro- and extended nano-dimensional features (Figure 2a, b). The micro-scale features were fabricated using positive photolithography followed by wet etching of the Si master to enable pattern transfer. For positive photolithography, AZ1518 resist was spin-coated onto the Si wafer at a thickness of 5 μm and exposed to UV light (365 nm) for 4 s. The non-polymerized resist was developed using MIF 300 and wet etching was done using 40% KOH to the desired depth with the chromium layer as the mask for the wet etching. The chromium layer was removed using a chromium etchant (Sigma-Aldrich). Finally, the extended nano-dimensional features of the XnCC were fabricated by focused ion beam (FIB; Quanta 3D Dual Beam System, FEI) milling using Ga ions [36–39]. Structures were milled with a beam current of 48 pA and a time of 1 μs. The final depths of the master mold were validated using metrology and a rapid scanning confocal microscope (Keyence) along with SEM; SEMs are shown in Figures 2c–d of the XnCC chip.

Poly-urethane acrylate (PUA resin; Minuta Technology) was used to replicate the structures from the Si master mold into the desired plastic, which in this case was cyclic olefin polymer (COP). The PUA resin was applied to the surface of the Si master mold and treated under a UV lamp with a power of 22 mW/cm^2 for 2.5 min. After UV curing, the stamp patterns were transferred to COP using thermal imprinting via nanoimprint lithography (NIL; Nanonex

2500) at 135 °C, 2.07 MPa for 5 min. The COP chip was then covered with a thin COC cover plate with both treated using an O_2 plasma for 2 min and thermal fusion bonded at 72 °C, 0.83 MPa for 15 min. We found that we could thermal imprint > 30 devices from a single resin stamp, and > 100 resin stamps could be made from a single Si master. Therefore, > 3,000 devices could be made from a single Si master negating the need for going back to the optical lithography and FIB milling to make additional Si masters.

2.2 COMOSOL Simulation

A 2D model of the XnCC was built-in AutoCAD and imported into COMSOL (V. 5.5) to evaluate the potential drop and electric field strength across the extended nanochannel and in-plane extended nanopore sensor. The electrolyte used was 1 × PBS, which is the same as that used in the experimental data. The Physics used was Electrostatics under AC/DC flow. A DC bias of −1 V was applied at one end of the microchannel, and the other end of the XnCC was grounded. A no-slip boundary condition was given to all boundaries, and a stationary study was adopted.

2.3 In-plane XnCC Device Setup and Data Analysis

XnCC chip priming and preparation steps are shown in Figure 3. The “low-pressure” side of the XnCC chip was filled with running buffer first, and then the “high-pressure” side was filled with the appropriate sample. A syringe pump was then connected to “Outlet II,” and “Outlet I” was sealed.

The withdrawal of sample originated from “Outlet II” to create hydrodynamic flow, and the sample streamed from the high-pressure side to the low-pressure side. Once fluidic connections were made, the chip was transferred to a Faraday cage and both electrodes were connected across the XnCC using two Ag/AgCl electrodes placed into reservoirs (Figure 3). The current amplifier circuitry (AxoPatch Clampex V10.1) was turned on for signal trace recordings. The voltage across the XnCC was set to −1 V, and based on simulations, the majority of the voltage drop occurred across the extended nanochannels and in-plane extended nanopore. From the 2D simulations, the in-plane nanopore had a steeper potential drop than within the nanochannels with about 10% of the potential drop occurring across the nanopore (Figure 4). The sampling frequency of the electronics was 100,000 Hz, and a 10 kHz lowpass filter was applied. The signal trace was recorded for 10 min and current traces were analyzed by Clampfit software. The trace background was zeroed and a post 400 Hz highpass filter was applied to reduce the noise level resulting from external electrical sources and the intrinsic noise of the electronics. The standard deviation in the background current trace was calculated based on an open-pore current, and a threshold condition was set at 5 × the standard deviation in the signal. The signals with higher amplitude than the threshold and longer duration than 0.02 ms were scored as events.

2.4 Fluorescent Beads for XnCC Characterization

A fluorescent bead mixture was used to evaluate the operational performance of the XnCC; 46 and 100 nm diameter polystyrene beads bearing a fluorescent label (AF 565; excitation maximum = 565; emission maximum = 580; Thermo Scientific; catalog numbers F8792 and F8800 for 0.04 and 0.1 μm particles, respectively) were mixed and diluted to a concentration

of ~ 4.7×10^{11} particles/mL, which was verified using nanoparticle tracking analysis (NTA). The bead mixture was passed through a 0.22 μm filter to remove aggregates and placed in the XnCC chip. The XnCC chip was imaged using a single-molecule tracking fluorescence microscope configured in an epi-illumination format that possessed a 532 nm green laser (Diode-pumped solid-state – Coherent; λ_{ex} = 532 nm; P = 2000 mW; 2 mm beam diameter; see Figure S1 in the SI for a schematic of this microscope), a 63 × objective, and Cy3 color channel used to visualize bead movement [26, 40, 41]; Figure 5 shows still images of bead movement through the in-plane nanopore sensor. The beads were analyzed optically using ImageJ. The events were collected from the electrical signal trace and analyzed for their size distribution as well using the in-plane extended nanopore sensor.

2.5 Calibration Curve for VP Counting

Pre-heated (to inactivate) SARS-CoV-2 VPs (ATCC) from cell culture media served as the stock solution and consisted of 3×10^8 particles/mL. The stock solution was diluted serially in 1 × PBS to establish a calibration curve. A total of ~ 30 μL of sample was filled into the XnCC chip. The sample was withdrawn at the receiving side of the in-plane extended nanopore sensor using a syringe pump with the electrodes connected across the in-plane extended nanopore sensor. The entire setup was placed in a Faraday cage and −1 V potential was applied. The electrical signals were recorded using an Axoptach 200B and analyzed using Clampfit 10.1 software. Each point of the standard curve was collected in duplicate and a different device was used for each measurement.

2.6 VP Recognition Using an Affinity Selection Chip

Four samples (saliva) were used to evaluate the performance of the XnCC chip for SARS-CoV-2 enumeration following affinity selection. Two saliva samples from donors whom tested negative for SARS-CoV-2 by RT-qPCR were spiked with heat-inactivated SARS-CoV-2 VPs (ATCC) to simulate positive COVID-19 samples. The other two saliva samples were not spiked with SARS-CoV-2 particles and served as blanks. The saliva samples were processed through a selection chip for SARS-CoV-2 VPs with the affinity agent consisting of a DNA aptamer targeting the spike protein (S protein) of SARS-CoV-2.[42] The aptamer was linked to the surface of the plastic chip using a coumarin-based photocleavable linker; the linker attachment to the plastic surface was enabled by UV/O_3 activating the plastic surface and using EDC/NHS coupling chemistry to allow for the covalent attachment (see Scheme S1 in the SI showing this chemistry).[42,43] The selection chip, which was made from a plastic using injection molding (see Figure S2 in the SI), consisted of ~1.5 M pillars that were 10 μm in diameter with a 10 μm edge-to-edge spacing.

Briefly, the aptamer attachment chemistry is explained here. After VP selection chip surface activation using UV/O_3 exposure, 2 mg/mL NHS and 20 mg/mL EDC in acetonitrile was infused into the chip and left at room temperature for 25 min. This was followed by introduction of a photocleavable linker into the chip, which was allowed to react at room temperature for 2 h [34]. This was followed by another EDC/NHS reaction in which the 5’ amino modified aptamer was added to the selection chip for attachment of the aptamer (see Scheme S1 in the SI).

For VP analysis, a wash buffer (1% PVP in 1× PBS) was pumped through the chip at a flow rate of 20 μL/min to eliminate non-specifically bound material to the chip's surfaces. Then, a 100 μL saliva sample was flowed through the chip at a rate of 10 μL/min, followed by a wash with 1 × PBS flowed through the chip at 15 μL/min. Following release of the selected VPs from the capture surface by a blue light LED, the released particles were analyzed by the XnCC chip.

2.7 EV Isolation from Mouse Plasma Samples

The EV selection chip fabrication and surface treatment have been described in previous publications [35, 44, 45]. After chip surface treatment using UV/O_3 activation, 2 mg/mL NHS and 20 mg/mL EDC in MES buffer (pH 5.0) was infused into the chip and left at room temperature for 25 min. Then, an antibody solution was infused into the chip and allowed to react at room temperature for 2 h. To minimize non-specific adsorption, mAb-modified selection chip surfaces were blocked with 1% PVP and 0.5% BSA in PBS (200 μL, 10 μL/min), then washed with 1% Tween20 in TBS after enrichment to remove non-specifically bound material [35]. As shown in ref. [35], verification of the isolation of CD8-bearing EVs using our selection chip was done by labeling the surface-captured EVs with a fluorescently-labeled anti-CD8 antibody with the proper controls. In this case, the antibodies were attached directly to the selection chip's surface and no photocleavable linker was used. Then, a 100 μL plasma sample was flowed through the chip at a flow rate of 10 μL/min, followed by a wash with 0.1% Tween-20 in 1 × TBS flowed through the chip at 15 μL/min. In one set of experiments, mouse plasma samples were analyzed using an anti-CD81 antibody (431301, R&D Systems) selection chip (see Figure S2), and the EVs were released by injecting 1 mg/mL proteinase K (Thermo Scientific) into the chip. The chip was incubated at 37 °C for 30 min and then rinsed using a washing buffer (0.1% Tween-20 in 1 × TBS) at a flow rate of 10 μL/min for 20 min. The effluent was stored at −80 °C and/or sent for enumeration. In the second set of experiments, EVs were selected using anti-CD8 antibodies.

2.8 EV Quantification Using BCA Assay

For some mouse plasma samples, the total protein content was analyzed by the BCA total protein assay to verify EV numbers. The BCA total protein assay was carried out using the Micro BCA Protein Assay Kit (Thermo Fisher Scientific). For this assay, ~30 μL of the effluent from the EV chip was used for the BCA assay, and the "Microplate Procedure" was used to determine the total protein from each sample, which could be correlated to the relative amount of EVs. A BSA (bovine serum albumin) protein standard was prepared with serial dilution to establish a calibration curve. The samples and standards were separately mixed with the working reagent at a 1:1 volume ratio and placed into a heating chamber at 37 °C for 2 h. The plate was then cooled to room temperature and set into a plate reader with 562 nm absorbance readout.

3 Results and Discussion

3.1 Evaluation of XnCC Chip Analytical Performance Using Fluorescent Beads

We set out to determine the analytical figures-of-merit of the XnCC chip using fluorescent beads so that we could correlate the electrical signals with observable fluorescent signals. For RPS current transients of fluorescent beads that were 46 and 100 nm in diameter, the event signal amplitudes ranged from 57 to 1203 pA, and the signal durations (formal width at half maximum, FWHM) ranged from 0.15 to 0.95 ms (Figures 6a, b, and d). For this data, the sampling rate was 100,000 Hz and the electronic bandwidth was set to 10 KHz on the Axopatch current amplifier. Therefore, even with a peak FWHM of 0.15 ms, we would expect to collect ~ 15 data points, which would indicate little if any peak distortion due to signal aliasing. However, the bandwidth of the electronics was set to 10 KHz, and thus we may expect some perturbation in peak amplitude for peaks with a FWHM < 0.1 ms. As can be seen from the event current trace shown in Figure 6d, the events provided positive polarity peaks with respect to the open pore current trace for this carrier electrolyte (1 × PBS) indicating that the fluorescent particles were more conductive than the carrier electrolyte.

The electrical signal amplitudes were histogrammed with a bin width of 100 pA. The histogram was fit to a normal distribution with two maxima (Figure 6e). This data indicated that we could detect both the 46 and 100 nm diameter nanoparticles and discriminate between them based on size. The bead mixture was also imaged using a fluorescence microscope (see Figure S1) to make sure the resultant electrical signals were indeed due to transport of beads through the in-plane extended nanopore sensor. Fluorescence intensities within the image were analyzed and the intensity was found to be proportional to the beads' sizes and were correlated to the electrical signals generated by the XnCC chip. The bead mixture's fluorescence amplitudes with respect to the electrical signal amplitudes from the XnCC chip were fit to a non-linear function and showed high correlation ($R = 0.9988$, $p < 0.0001$) confirming that our electrical signals originated from beads traveling through the in-plane extended nanopore sensor (Figure 6c).

The average diameter and the size distribution for these particles, as per manufacturer certificate of analysis, was 46 ± 6.4 nm (RSD = 13.9%) and 100 ± 12 nm (RSD = 12.0%). The electrical signals as generated in the RPS data for these particles were found to be 454.2 ± 94.3 pA (RSD = 20.8%) and 779.4±52.1 pA (RSD = 6.7%) for the 46 nm and 100 nm particles, respectively. The size distribution of these beads from the manufacturer's data was slightly smaller than the RSD for the RPS signal generated for 46 nm particles. This likely represents a consequence of "off-axis" effects in our XnCC device. This effect depends on the ratio of the particle volume to the volume of the extended nanopore, and will be more pronounced for smaller particles because a shift in position with respect to the boundary conditions imposed by the XnCC [46].

For the volume flow rate, the range of particle's FWHM was from 0.15 to 0.95 ms for an effective pore length of ~225 nm (see Figure 4f), a volume flow rate of 3.13×10^{-11} mL/s was determined (for particle FWHM of 0.15 ms). Therefore, we could estimate the particle's size from the amplitude of the current transients and the transient width allowed

us to determine the volume flow rate and with the event frequency, the bead concentration could be deduced (Figure 6d, e).

3.2 SARS-CoV-2 Particle Counting by nCC Chip

As a demonstration of the XnCC for label-free counting of affinity-selected particles, we used the analysis of SARS-CoV-2 VPs associated with COVID-19. Corona-viruses (CoVs) are a family of enveloped viruses with a size ~ 125 nm in diameter and contain a single-stranded RNA genome.[47–51] We used a microfluidic chip with its surfaces containing an aptamer that targeted the receptor binding domain of the spike protein to affinity select these VPs from biological samples, in this case saliva [42]. The SARS-CoV-2 VPs were released from the capture surface and collected in the output reservoir of this chip (volume = 30 μL), which was pipetted out of this reservoir and loaded into the XnCC chip for label-free enumeration. The XnCC chip was used to perform SARS-CoV-2 VP counting, which has an average particle size of ~121 nm (range = 50–200 nm) as determined by nanoparticle tracking analysis (NTA) of a stock solution of SARS-CoV-2.

For these investigational studies, we seeded SARS-CoV-2 VPs (heat inactivated from ATCC; L strain from Wuhan, China) into saliva samples at known concentrations. Because the XnCC is a universal detector and counts any particle with the appropriate size range (40 nm–200 nm, set by the smallest particle we can detect based on SNR considerations as seen in Figure 6, and the size of the in-plane pore, respectively) for the analysis of saliva, a pre-selection process must be undertaken to remove endogenous particles from the sample that may interfere with the measurement, for example EVs that can be found in saliva [52]. The selection chip used here consisted of a plastic chip with a high density array of micropillars (~ 1.5 M pillars) that served as the solid support for selecting the VPs specifically from the saliva sample through the use of an affinity agent, in this case an aptamer. Following selection of the target VPs, they could be released from the capture surface using blue light that photocleaves the coumarin linker (see Figure S2 in SI as well as Scheme S1).

Before counting the VPs from saliva samples, a standard curve was established to evaluate the XnCC chip's analytical figures-of-merit for the SARS-CoV-2 VPs by serial dilution of a stock solution (Figure 7a – b). An expanded view of a single RPS event and the PBS background are shown in Figures 7c–d. Each dilution was run in duplicate, and the standard curve was fit to a linear function and a correlation coefficient of 0.9714 was found (Figure 7e). For this XnCC chip, the limit-of-detection was determined to be 5.8×10^{6} particles mL^{-1} (signal-to-noise ratio = 5). From the input load and the number of detected signals, we estimated the sampling efficiency (*i. e.*, percentage of particles that actually travel through the single pore with respect to those that flow through the XnCC chip) to be ~1.5×10^{-4}%. This low sampling efficiency results from the use of a single pore with an effective diameter of 200 nm and a relatively large adjoining microchannel. In addition, the small pressure drop across the pore created by the pulling action of the syringe on the receiving side of the pore reduced the sampling efficiency as well. We should note that the detection efficiency is ~ 100% (this was deduced from the effective sampling length of the pore [225 nm, see Figure 4], the average transit time of particles through the pore [~0.5 ms], the sampling time [300s],

the particle number per unit volume [5.5×10^8 particles per mL], and the number of events detected [371]).

We tested the nCC to enumerate VPs spiked into saliva samples (Figure 7f). In these samples, the SARS-CoV-2 concentration for samples 1 and 2 were 5.5×10^8 and 2.1×10^8 particles/mL, respectively, while samples 3 and 4 had no particles added into the saliva (*i.e.*, all four saliva samples were found to be negative for COVID-19 as determined by RT-qPCR while the positive controls gave discernible RT-qPCR signals, see Figure S3 in the SI). As can be seen from Figure 7f, events were clearly detected in the positive controls (samples 1, 2) with no particles detected in the negative controls (samples 3, 4). The results showed that the XnCC chip is capable of enumerating SARS-CoV-2 VPs specifically when coupled to a chip for affinity selection of the desired target. However, in this case the viral loads for the positive controls were high (~10^8 particles per mL) and thus, further optimization of the XnCC is necessary to quantify the VPs for COVID-19 when the viral load is low; the viral load for COVID-19 patients using saliva testing can range from 10^3–10^8 particles per mL [53].

3.3 CD81 and CD8 EVs for Determining Radiation Exposure

In the second application example of the XnCC, our goal was to establish an assay that coupled EV isolation and enumeration to detect and monitor the status of radiation exposure levels in patients. Accidental radiation exposure has been recognized as a disaster caused by humans with > 90 nuclear and radiation accidents occurring over the past 60 years [54, 55]. Governments have spent > $20 billion for recovery from accidental radiation exposure [56–58]. In addition, there have been numerous deaths directly or indirectly resulting from ionizing radiation [59–61]. During triage to understand patient exposure levels, the attending physician can only estimate radiation injury level by questioning the patient as to exposure details [62].

In these proof-of-concept studies, a mouse model was used for these studies and consisted of non-exposed, low dose (2 Gy), and high dose (12 Gy) exposed mice. A microfluidic chip was used for EV affinity isolation of CD8 expressing EVs from mouse plasma samples [35]. Previous work has shown that the cellular activity of CD8+ T cells can be induced by radiation [63–65], and thus, CD8-expressing EVs can potentially be used as a biomarker of radiation exposure.

The risk of radiation exposure from detonation of nuclear weapons, terrorist attacks on nuclear reactors, or the use of conventional explosives to disperse radioactive substances has increased in recent years. To ensure efficient use of medical resources following a radiological incident, there is an urgent need for simple assays to determine the degree of exposure. These assays should determine after exposure to ionizing radiation changes in biological endpoints via informative biomarkers that are easily accessible. In the case of large-scale radiological accidents, these biomarkers could be used to identify individual exposure cases. In some situations, triage decisions have to be undertaken as soon as possible to parse exposed subjects into different categories depending on their exposure dose and radio-sensitivity; this type of information is typically not secured from a simple Geiger counter measurement.

An immune system-related marker, CD8, and an EV marker, CD81 (*i.e.*, tetraspanin), were used as capture elements of EVs from plasma samples. The goal of these proof-of-concept studies was to determine if we could use the selection chip described above (see Figure S2) to affinity select EVs from samples, release the selected EVs, and enumerate them to serve as an analysis strategy to determine the extent of radiation exposure of subjects. As a note, we have shown that our XnCC can detect particles with an average size of 46 nm (see Figure 6e), but the size distribution of EVs isolated using our selection chip has been shown to range from ~35 nm to 400 nm [35]. Therefore, we can possibly not detect EVs < 40 nm in diameter and those with diameters > 200 nm can block the pore. However, in no case did we notice device failure due to EV blockage.

Our first step was to identify which affinity marker was best suited to distinguish between non-exposure, high, and low dose conditions could be distinguished and thus, we evaluated two different ones herein: (i) CD81, which collects the entire population of exosomes irrespective of their cell-of-origin because CD81 is a tetraspanin ubiquitously found in most exosomes. (ii) Literature precedence has also shown that radiation exposure will induce cellular activity of CD8 expressing T cells [63, 65–69]. As a result, higher levels CD8+ T cell-related circulating EVs may be expected for radiation exposed subjects because of increased T-cell activity. Model studies were performed in mice exposed to sub-lethal and lethal doses of radiation (no exposure, 2 Gy, and 12 Gy). Radiation was delivered to 8–10 week-old male C57BL6 mice using a small animal radiation research platform (Xenx; XStrahl, Surrey, UK). Following exposure, the mice were sacrificed and the plasma analyzed for levels of CD8 EVs or CD81 expressing exosomes. In these experiments, 30 plasma samples were analyzed including 10 non-exposed mice, 10 low dose exposed mice (2 Gy), and 10 high dose exposed mice (10 Gy). At 24 h post irradiation, mice were euthanized and blood was collected from which plasma was isolated.

Mouse plasma samples were first analyzed using the anti-CD81 antibody selection chip. For this analysis, neither exosome quantity nor size showed significant differences between non-exposed and radiation exposed mice (Figure 8a, b). However, based on the literature the prodromal stage of ionizing radiation is 4 to 24 h, and the level of circulating EV production may peak after 6 h [70–73]. Therefore, we performed a second set of experiments that included analysis of plasma samples in mice 6 h and 24 h post-radiation exposure. However, there were no differences in EV quantity or size for exposed and non-exposed mice (see Figure S4 in SI) when using anti-CD81 antibodies for exosome selection from plasma. For the EVs isolated using anti-CD81 antibodies, the entire exosome population was selected by the chip [74–76]. The total exosome population in plasma might be at similar levels due to the higher uptake rate with post-radiation exposure [77].

We next performed experiments directed toward evaluating CD8 expressing EVs with respect to radiation exposure. As shown in Figure 8c and d, the CD8-related EVs for the low dose and high dose groups exhibited significantly higher EV levels compared to the control group that received no radiation exposure ($p=0.0076$ and $p=0.0001$, respectively). These results indicated that CD8-related EVs were upregulated in both of the low-dose and high-dose groups and both were higher than the non-exposed mice, which was not the case for the CD81-expressing exosomes. We should note that the CD8 expressing EVs could express

CD81 as well and Western blotting could determine if there were co-expression. However, the fact that anti-CD81 antibodies can select all exosomes, even those not originating from T-cells may mask the subtle EV changes induced by radiation exposure.

3.4 RPS Signal Polarity and Analysis

The XnCC chip generated both positive (EVs and polystyrene beads) and negative (VPs) polarity pulses compared to 1 × PBS buffer in our electrical signals but not just negative polarity pulses as most RPS data show [1–4, 78]. For RPS with a constant potential applied across the pore, non-conductive particles will increase the resistance when resident within the pore, producing negative polarity peaks. However, in the case of conductive particles, they can carry more ions than the surrounding electrolyte increasing the conductivity when a particle is resident within the pore and thus, result in a positive polarity signals [1]. In our case, we are using 1 × PBS as the carrier electrolyte without 1 M KCl spiked into the carrier electrolyte as is typically done in RPS experiments, which will produce a lower conductivity open pore current.

For the bead experiments, polystyrene was the bead material and literature has shown that polystyrene beads can provide positive polarity events in RPS because of the porous nature of the beads [8, 79–82], which creates significantly higher surface area than a non-porous bead. The porous beads will carry more ions due to the larger surface area, generating an increased charge/volume ratio. As a result, the ionic concentration in the bead can be higher than the ionic concentration in the surrounding carrier electrolyte and thus results in positive-polarity events. The EVs when counted using the nCC chip with 1× PBS also showed positive polarity events. Due to the small size of the extended nanopore, the electrical field strength can be as high as 10 kV/cm, and particles translocated through the pore in ~0.5 ms. With such a high electrical field strength and short translocation duration, the pore can provide an electroporation condition for a phospholipid bilayer comprising the EV membrane. Thus, the EV membrane can become permeable due to possible electroporation, and the vesicles with a permeable membrane would result in a higher conductivity when the surrounding buffer condition was 1 × PBS.[83,84] However, inspection of the current transient data showed that the SARS-CoV-2 VPs generated negative polarity peaks indicating that electroporation was probably not present under the nCC operating conditions employed here.

4 Conclusions

In this manuscript, we demonstrated the use of an inplane extended nanopore sensor fabricated in a thermoplastic for enumerating VPs and EVs affinity selected from a plastic chip. Conventional methods for the analysis of EVs and VPs uses NTA and/or electron microscopy for enumeration, which has significant drawbacks such as large variability and sample selection bias [85,86], complicated workflows that require specialized operators, and highly sophisticated equipment. The XnCC chip discussed herein offers some unique advantages for the analysis of biological particles including small sample consumption (< 30 μL), label-free detection using simple instrumentation, large dynamic range (10^3 to 10^8 particles/mL), and the potential for mass production of the chip via injection

molding because of the fact that it was made from a thermoplastic, in this case COP. Thermoplastics not only offer the ability to be produced in a high production mode and at low-cost using injection molding, but also have favorable surface chemistries for microfluidic applications. For example, COP can be O_2 plasma activated in a similar fashion as PDMS to reduce its water contact angle to make the surface more wettable to minimize bubble formation, generate stable electroosmotic flow, and reduce non-specific adsorption artifacts especially in high surface-area-to-volume ratio devices as that associated with our XnCC. Unfortunately, PDMS shows rapid hydrophobic recovery to its pre-oxidized water contact angle (112°) in < 2 days due to its low glass transition temperature (−120 °C) [87] as compared to COP (glass transition temperature = 102 °C), which shows minimal water contact angle changes (30°→38° over a 25 day period). While the rapid hydrophobic recovery can be mitigated in PDMS using surface modification chemistries [87], it adds cost and time to device production. In our case, the COP-based device is molded, O_2 plasma oxidized and thermally bonded only.

The XnCC chip could analyze particles from 40 to 200 nm in diameter and do so using simple instrumentation and in a label free fashion. Unique to our XnCC chip was the use of an in-plane pore integrated to a fluidic network and the fact that the device was made in a thermoplastic (COP) via imprinting. An excellent correlation was found between the electrical signal generated by fluorescently-labeled polystyrene beads and the optical signal secured using a fluorescence microscope verifying the electrical signals detected were indeed due to the particles traveling through the pore. Also, the histogram of the beads' electrical signal showed two peaks with each following a normal distribution confirming two size distributions measured, which were 46 nm and 100 nm corresponding to the particles seeded into the carrier electrolyte.

However, the universal detection nature of the XnCC chip when processing complex biological samples required a selection process prior to enumeration and for this we used a selection chip to affinity select targets prior to counting to afford high specificity in the measurement. We successfully characterized both saliva samples for VPs and mouse plasma samples for EVs. Applications were established using the selection and XnCC chips in combination, including identifying radiation injury and the enumeration of SARS-CoV-2 VPs. The results and data from irradiated mice indicated that CD8-associated EVs showed high EV numbers but this was not the case for the CD81-expressing EVs (see Figure 8). In this condition, CD8+ T cells may increase in cellular activity in the presence of radiation injury, which includes serving as a repair mechanism of damaged cells. The high level of cellular activity increased the secretion of CD8 EVs [88, 89].

Our XnCC chip also has the capability to count particles <200 nm in size, and was adapted for SARS-CoV-2 VP counting using an aptamer as the affinity agent attached to the surface of a plastic chip containing ~ 1.5 M pillars. This pillared chip and the aptamer showed high specificity as it did not capture other human corona viruses, for example HCoV-OC43 and HCoV-229E. In addition, the selection of SARS-CoV-2 from saliva was verified using RT-qPCR (see Figure S3). In the four saliva samples tested, the XnCC chip was able to determine the concentration of VPs following upstream selection and release from the capture surface. However, the current performance of the XnCC chip for SARS-CoV-2

enumeration may still require further optimization to lower the concentration LOD due to the low levels of VPs found in saliva samples for some infected individuals; this limitation resulted from issues associated with the sampling efficiency and not the detection efficiency. We are in the process of improving the concentration LOD for this sensing platform by improving the sampling efficiency.

We are also working on integrating the two chips into a single unit using a modular microfluidic format [90–94] and miniaturizing the control electronics for realizing field use of this platform technology for point-of-care testing in both application scenarios. For example, at-home testing for infectious diseases and a bio-dosimeter for triaging radiation exposed individuals. Bio-dosimeter information will allow focusing the medical staff and facilities only on those individuals in need of urgent medical assistance. At present, there is no bio-dosimeter approved by the FDA. Moreover, there are no devices available to perform this rapid initial triage at the point-of-care.

Supplementary Material

Refer to Web version on PubMed Central for supplementary material.

Acknowledgements

The authors would like to thank the NIH for financial support of this work (NIH RADx program; NIBIB P41-EB020594; and P20-GM130423).The authors also acknowledge the KU Nanofabrication Facility (KUNF, P20-GM103638). We also acknowledge the National Institute of General Medical Sciences of the National Institutes of Health P20-GM113117.

We would like to dedicate this manuscript to the contributions of Prof. Theodore Kuwana (TK) to the field of electrochemistry and analytical chemistry. Unfortunately, TK passed away in December of 2021. TK was the inventor of spectroelectrochemistry and made invaluable contributions to the area carbon electrodes from both a fundamental and translational perspective as well as many other areas of analytical chemistry. TK was the consummate mentor, whom fostered a number of graduate students and post-docs that have also made important contributions to the field of analytical chemistry. TK was the PhD advisor of SAS and made an impactful contribution to his career as well as the many students that have been and continue to be trained by SAS, both graduate and undergraduate students. As a testament to the tight family of TK, both MLH and MAW, whom are co-authors on this manuscript, were graduate students under the direction of Prof. Greg Swain (PhD student of TK) and did post-graduate work with Prof Steven A Soper, also a PhD student of TK.

Data Availability Statement

Data available on request from the authors.

References

[1]. Kozak D, Anderson W, Vogel R, Trau M, Nano Today 2011, 6, 531–545. [PubMed: 22034585]

[2]. Song Y, Zhang J, Li D, Micromachines (Basel) 2017, 8.

[3]. Vaclavek T, Prikryl J, Foret F, J. Sep. Sci 2019, 42, 445–457. [PubMed: 30444312]

[4]. Willmott GR, Anal. Chem 2018, 90, 2987–2995. [PubMed: 29441785]

[5]. DeBlois RW, Uzgiris EE, Cluxton DH, Mazzone HM, Anal. Biochem 1978, 90, 273–288. [PubMed: 727469]

[6]. Anderson W, Lane R, Korbie D, Trau M, Langmuir 2015, 31, 6577–6587. [PubMed: 25970769]

[7]. DeBlois RW, Wesley RK, Virol J. 1977, 23, 227–233.

[8]. Lan W-J, Xiong CKJ-W, Bund A, White HS, J. Phys. Chem. C 2014, 118, 2726–2734.

[9]. Pan R, Hu K, Jiang D, Samuni U, Mirkin MV, J. Am. Chem. Soc 2019, 141, 19555–19559. [PubMed: 31771324]

[10]. Arima A, Tsutsui M, Harlisa IH, Yoshida T, Tanaka M, Yokota K, Tonomura W, Taniguchi M, Okochi M, Washio T, Kawai T, Sci. Rep 2018, 8, 16305. [PubMed: 30390013]

[11]. Heider S, Metzner C, Virology 2014, 462–463, 199–206.

[12]. Fraikin JL, Teesalu T, McKenney CM, Ruoslahti E, Cleland AN, Nat. Nanotechnol 2011, 6, 308–313. [PubMed: 21378975]

[13]. Yang L, Yamamoto T, Front. Microbiol 2016, 7, 1500. [PubMed: 27713738]

[14]. Song Y, Zhang H, Chon CH, Chen S, Pan X, Li D, Anal. Chim. Acta 2010, 681, 82–86. [PubMed: 21035606]

[15]. Golichenari B, Nosrati R, Farokhi-Fard A, Faal Maleki M, Gheibi Hayat SM, Ghazvini K, Vaziri F, Behravan J, Crit. Rev. Biotechnol 2019, 39, 1056–1077. [PubMed: 31550916]

[16]. Wang Y, Kececi K, Mirkin MV, Mani V, Sardesai N, Rusling JF, Chem. Sci 2013, 4, 655–663. [PubMed: 23991282]

[17]. Chavis AE, Brady KT, Hatmaker GA, Angevine CE, Kothalawala N, Dass A, Robertson JWF, Reiner JE, ACS Sens. 2017, 2, 1319–1328. [PubMed: 28812356]

[18]. Zhou T, Song Y, Yuan Y, Li D, Anal. Chim. Acta 2019, 1052, 113–123. [PubMed: 30685029]

[19]. Guo J, Huang X, Ai Y, Anal. Chem 2015, 87, 6516–6519. [PubMed: 26035335]

[20]. Song Y, Li M, Pan X, Wang Q, Li D, Electrophoresis 2015, 36, 398–404. [PubMed: 25146579]

[21]. Sexton LT, Mukaibo H, Katira P, Hess H, Sherrill SA, Horne LP, Martin CR, J. Am. Chem. Soc 2010, 132, 6755–6763. [PubMed: 20411939]

[22]. Sexton LT, Horne LP, Sherrill SA, Bishop GW, Baker LA, Martin CR, J. Am. Chem. Soc 2007, 129, 13144–13152. [PubMed: 17918938]

[23]. Blundell EL, Vogel R, Platt M, Langmuir 2016, 32, 1082–1090. [PubMed: 26757237]

[24]. Booth MA, Vogel R, Curran JM, Harbison S, Travas-Sejdic J, Biosens. Bioelectron 2013, 45, 136–140. [PubMed: 23455053]

[25]. Saleh OA, Sohn LL, Nano Lett. 2003, 3, 37–38.

[26]. Amarasekara CA, Athapattu US, Rathnayaka C, Choi J, Park S, Soper SA, Electrophoresis 2020, 41.

[27]. Zhou K, Li L, Tan Z, Zlotnick A, Jacobson SC, J. Am. Chem. Soc 2011, 133, 1618–1621. [PubMed: 21265511]

[28]. Harms ZD, Selzer L, Zlotnick A, Jacobson SC, ACS Nano 2015, 9, 9087–9096. [PubMed: 26266555]

[29]. Xu Y, Adv. Mater 2018, 30, 1702419.

[30]. Becker H, Lab Chip 2009, 9, 2759–2762. [PubMed: 19967108]

[31]. Jackson JM, Witek MA, Kamande JW, Sope SA, Chem. Soc. Rev 2017, 46, 4245–4280. [PubMed: 28632258]

[32]. Ayala-Mar S, Donoso-Quezada J, Gallo-Villanueva RC, Perez-Gonzalez VH, Gonzalez-Valdez J, Electrophoresis 2019, 40, 3036–3049. [PubMed: 31373715]

[33]. Nair SV, Witek MA, Jackson JM, Lindell MAM, Hunsucker SA, Sapp T, Perry E, Hupert ML, Bae-Jump V, Gehrig PA, Wysham WZ, Armistead PM, Voorhees P, Soper SA, Chem. Commun 2015, 51, 3266–3269.

[34]. Pahattuge TN, Jackson M, Digamber R, Wijerathne H, Brown V, Witek MA, Perera C, Givens RS, Peterson BR, Soper SA, Chem. Commun 2020, 56, 4098–4101.

[35]. Wijerathne H, Witek MA, Jackson JM, Brown V, Hupert ML, Herrera K, Kramer C, Davidow AE, Li Y, Baird AE, Murphy MC, Soper SA, Commun. Biol 2020, 3, 613. [PubMed: 33106557]

[36]. Athapattu US, Rathnayaka C, Vaidyanathan S, Gamage SST, Choi J, Riahipour R, Manoharan A, Hall AR, Park S, Soper SA, ACS Sens. 2021, 6, 3133–3143. [PubMed: 34406743]

[37]. Chantiwas R, Hupert ML, Pullagurla SR, Balamurugan S, Tamarit-Lopez J, Park S, Datta P, Goettert J, Cho YK, Soper SA, Lab Chip 2010, 10, 3255–3264. [PubMed: 20938506]

[38]. Chantiwas R, Park S, Soper SA, Kim BC, Takayama S, Sunkara V, Hwang H, Cho YK, Chem. Soc. Rev 2011, 40, 3677–3702. [PubMed: 21442106]

[39]. Wu JH, Chantiwas R, Soper SA, Park SA, Fabrication of Cost-effective Polymer-based Nanofluidic Device for Single Molecular Analysis, 2012.

[40]. Amarasekara CA, Rathnayaka C, Athapattua US, Zhang L, Choi J, Park S, Nagel AC, Soper SA, J. Chromatogr. A 2021, 1638, 461892. [PubMed: 33477027]

[41]. O'Neil C, Amarasekara CA, Weerakoon-Ratnayake KM, Gross B, Jia Z, Singh V, Park S, Soper SA, Anal. Chim. Acta 2018, 1027, 67–75. [PubMed: 29866271]

[42]. Song Y, Song J, Wei X, Huang M, Sun M, Zhu L, Lin B, Shen H, Zhu Z, Yang C, Anal. Chem 2020, 92, 9895–9900. [PubMed: 32551560]

[43]. Pahattuge TN, Jackson JM, Digamber R, Wijerathne H, Brown V, Witek MA, Perera C, Givens RS, Peterson BR, Soper SA, Chem. Commun 2020, 56, 4098–4101.

[44]. Hupert ML, Jackson JM, Wang H, Witek MA, Kamande J, Milowsky MI, Whang YE, Soper SA, Microsyst Technol 2014, 20, 1815–1825. [PubMed: 25349469]

[45]. Harshani Wijerathne MAW, Mateusz LH, Jackson JM, Soper SA, 2019.

[46]. Berge LI, Jsssang T, Feder J, Meas. Sci. Technol 1990, 1, 471–474.

[47]. Cui J, Li F, Shi ZL, Nat. Rev. Microbiol 2019, 17, 181–192. [PubMed: 30531947]

[48]. Bárcena M, Oostergetel GT, Bartelink W, Faas FG, Verkleij A, Rottier PJ, Koster AJ, Bosch BJ, Proc. Natl. Acad. Sci. USA 2009, 106, 582–587. [PubMed: 19124777]

[49]. Neuman BW, Adair BD, Yoshioka C, Quispe JD, Orca G, Kuhn P, Milligan RA, Yeager M, Buchmeier MJ, J. Virol 2006, 80, 7918–7928. [PubMed: 16873249]

[50]. Wang Y, Sun J, Zhu A, Zhao J, Zhao J, J. Thorac. Dis 2018, 10, S2260. [PubMed: 30116605]

[51]. Chen B, Tian EK, He B, Tian L, Han R, Wang S, Xiang Q, Zhang S, El Arnaout T, Cheng W, Signal Transduct Target Ther 2020, 5, 89. [PubMed: 32533062]

[52]. LeClaire M, Gimzewski J, Sharma S, Nano Select 2021, 2, 1–15.

[53]. Kim YG, Yun SG, Kim MY, Park K, Cho CH, Yoon SY, Nam MH, Lee CK, Cho YJ, Lim CS, J. Clin. Microbiol 2017, 55, 226–233. [PubMed: 27807150]

[54]. Rojavin Y, Seamon MJ, Tripathi RS, Papadimos TJ, Galwankar S, Kman N, Cipolla J, Grossman MD, Marchigiani R, Stawicki SP, J Emerg Trauma Shock 2011, 4, 260–272. [PubMed: 21769214]

[55]. Clement CH, Ann. ICRP 2016, 45, 4–6. [PubMed: 28952353]

[56]. Matzo M, Wilkinson A, Lynn J, Gatto M, Phillips S, Biosecur Bioterror 2009, 7, 199–210. [PubMed: 19635004]

[57]. Mettler FA Jr., Voelz GL, N. Engl. J. Med 2002, 346, 1554–1561. [PubMed: 12015396]

[58]. Gerber TC, Carr JJ, Arai AE, Dixon RL, Ferrari VA, Gomes AS, Heller GV, McCollough CH, McNitt-Gray MF, Mettler FA, Mieres JH, Morin RL, Yester MV, Circulation 2009, 119, 1056–1065. [PubMed: 19188512]

[59]. Burgio E, Piscitelli P, Migliore L, Int. J. Environ. Res. Public Health 2018, 15.

[60]. DiCarlo AL, Maher C, Hick JL, Hanfling D, Dainiak N, Chao N, Bader JL, Coleman CN, Weinstock DM, Disaster Med Public Health Prep 2011, 5 Suppl 1, S32–44. [PubMed: 21402810]

[61]. Koenig KL, Goans RE, Hatchett RJ, Mettler FA Jr., Schumacher TA, Noji EK, Jarrett DG, Ann Emerg Med 2005, 45, 643–652. [PubMed: 15940101]

[62]. Kunkler J, Adams TG, Manger M, Casagrande R, Health Phys. 2018, 115, 308–312. [PubMed: 29889700]

[63]. Filatenkov A, Baker J, Mueller AM, Kenkel J, Ahn GO, Dutt S, Zhang N, Kohrt H, Jensen K, Dejbakhsh-Jones S, Shizuru JA, Negrin RN, Engleman EG, Strober S, Clin. Cancer Res 2015, 21, 3727–3739. [PubMed: 25869387]

[64]. Bristol JA, Schlom J, Abrams SI, J. Immunol 1998, 160, 2433–2441. [PubMed: 9498787]

[65]. Lee Y, Auh SL, Wang Y, Burnette B, Wang Y, Meng Y, Beckett M, Sharma R, Chin R, Tu T, Weichselbaum RR, Fu YX, Blood 2009, 114, 589–595. [PubMed: 19349616]

[66]. Garnett CT, Palena C, Chakraborty M, Tsang KY, Schlom J, Hodge JW, Cancer Res. 2004, 64, 7985–7994. [PubMed: 15520206]

[67]. Chakraborty M, Abrams SI, Camphausen K, Liu K, Scott T, Coleman CN, Hodge JW, J. Immunol 2003, 170, 6338–6347. [PubMed: 12794167]

[68]. Zheng L, Li Z, Ling W, Zhu D, Feng Z, Kong L, Cell. Physiol. Biochem 2018, 46, 740–756. [PubMed: 29621784]

[69]. McKelvey KJ, Hudson AL, Back M, Eade T, Diakos CI, Mamm. Genome 2018, 29, 843–865. [PubMed: 30178305]

[70]. Webb RL, Kaiser EE, Jurgielewicz BJ, Spellicy S, Scoville SL, Thompson TA, Swetenburg RL, Hess DC, West FD, Stice SL, Stroke 2018, 49, 1248–1256. [PubMed: 29650593]

[71]. Jelonek K, Widlak P, Pietrowska M, Protein Pept. Lett 2016, 23, 656–663. [PubMed: 27117741]

[72]. Yentrapalli R, Merl-Pham J, Azimzadeh O, Mutschelknaus L, Peters C, Hauck SM, Atkinson MJ, Tapio S, Moertl S, Int. J. Radiat. Biol 2017, 93, 569–580. [PubMed: 28264626]

[73]. Kulkarni S, Koller A, Mani KM, Wen R, Alfieri A, Saha S, Wang J, Patel P, Bandeira N, Guha C, Chen EI, Int. J. Radiat. Oncol. Biol. Phys 2016, 96, 566–577. [PubMed: 27485285]

[74]. Tian Y, Ma L, Gong M, Su G, Zhu S, Zhang W, Wang S, Li Z, Chen C, Li L, Wu L, Yan X, ACS Nano 2018, 12, 671–680. [PubMed: 29300458]

[75]. Tauro BJ, Greening DW, Mathias RA, Ji H, Mathivanan S, Scott AM, Simpson RJ, Methods 2012, 56, 293–304. [PubMed: 22285593]

[76]. Jeppesen DK, Hvam ML, Primdahl-Bengtson B, Boysen AT, Whitehead B, Dyrskjot L, Orntoft TF, Howard KA, Ostenfeld MS, J Extracell Vesicles 2014, 3, 25011. [PubMed: 25396408]

[77]. Hazawa M, Tomiyama K, Saotome-Nakamura A, Obara C, Yasuda T, Gotoh T, Tanaka I, Yakumaru H, Ishihara H, Tajima K, Biochem. Biophys. Res. Commun 2014, 446, 1165–1171. [PubMed: 24667602]

[78]. Qiu Y, Siwy Z, Nanoscale 2017, 9, 13527–13537. [PubMed: 28871289]

[79]. Menestrina J, Schiel CYM, Vlassiouk I, Siwy ZS, The Journal of Physical Chemistry C 2014, 118, 2391–2398.

[80]. Cabello-Aguilar S, Abou Chaaya A, Picaud F, Bechelany M, Pochat-Bohatier C, Yesylevskyy S, Kraszewski S, Bechelany MC, Rossignol F, Balanzat E, Janot JM, Miele P, Dejardin P, Balme S, Phys. Chem. Chem. Phys 2014, 16, 17883–17892. [PubMed: 25045766]

[81]. Innes LM, Chen CH, Schiel M, Pevarnik M, Haurais F, Toimil-Molares ME, Vlassiouk I, Theogarajan L, Siwy ZS, Anal. Chem 2014, 86, 10445–10453. [PubMed: 25245282]

[82]. Goyal G, Freedman KJ, Kim MJ, Anal. Chem 2013, 85, 8180–8187. [PubMed: 23885645]

[83]. Sweeney DC, Douglas TA, Davalos RV, Technol. Cancer Res. Treat 2018, 17, 1533033818792490. [PubMed: 30231776]

[84]. Garcia-Sanchez T, Muscat A, Leray I, Mir LM, Bioelectrochemistry 2018, 119, 227–233. [PubMed: 29107172]

[85]. Srivastava A, Filant J, Moxley KM, Sood A, McMeekin S, Ramesh R, Curr. Gene Ther 2015, 15, 182–192. [PubMed: 25537774]

[86]. van der Pol E, Coumans FA, Grootemaat AE, Gardiner C, Sargent IL, Harrison P, Sturk A, van Leeuwen TG, Nieuwland R, J. Thromb. Haemostasis 2014, 12, 1182–1192. [PubMed: 24818656]

[87]. Zhou J, Ellis AV, Voelcker NH, Electrophoresis 2010, 31, 2–16. [PubMed: 20039289]

[88]. Barile L, Vassalli G, Pharmacol. Ther 2017, 174, 63–78. [PubMed: 28202367]

[89]. Raposo G, Stoorvogel W, J. Cell Biol 2013, 200, 373–383. [PubMed: 23420871]

[90]. You BH, Chen PC, Park DS, Park S, Nikitopoulos DE, Soper SA, Murphy MC, J. Micromech. Microeng 2009, 19.

[91]. You BH, Park DS, Chen PC, Rani SD, Nikitopoulos DE, Soper SA, Murphy MCA, Assembly tolerance analysis for injection molded modular, polymer microfluidic devices 2009.

[92]. Wang H, Chen HW, Hupert ML, Chen PC, Datta P, Pittman TL, Goettert J, Murphy MC, Williams D, Barany F, Soper SA, Angew. Chem. Int. Ed 2012, 51, 4349–4353;Angew. Chem 2012, 124, 4425–4429.

[93]. Chen YW, Wang H, Hupert M, Soper SA, Analyst 2013, 138, 1075–1083. [PubMed: 23308354]

[94]. Chen YW, Wang H, Hupert M, Witek M, Dharmasiri U, Pingle MR, Barany F, Soper SA, Lab Chip 2012, 12, 3348–3355. [PubMed: 22859220]

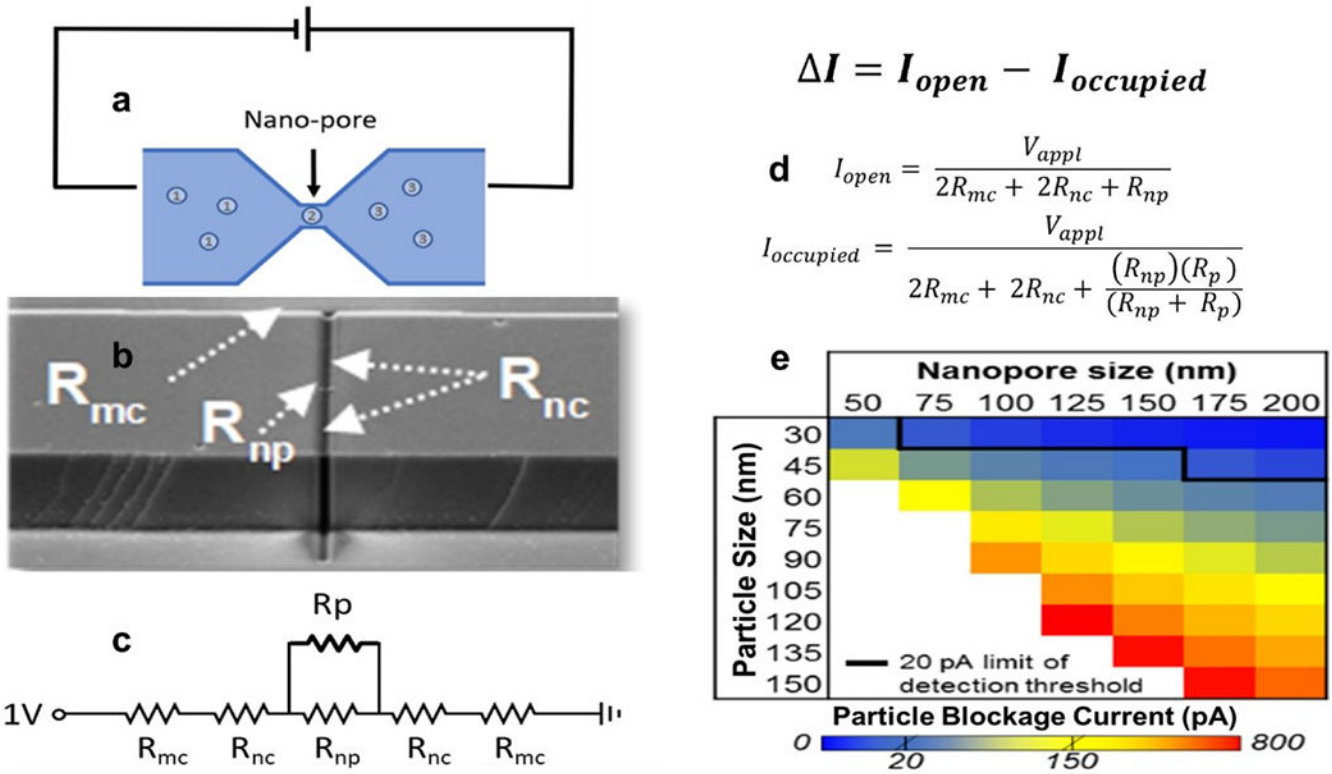

Fig. 1.

Operation of the extended nano-Coulter counter (XnCC) chip. **(a)** Schematic showing the in-plane pore of theX nCC along with the connecting nanochannel that flanks both sides of the pore. Whenever a particle travels through the in-plane pore sensor, an electrical signal is generated due to blockage (resistive pulse peak) of the pore by the particle. The particle size and concentration can be measured by analyzing the current amplitude and frequency of the resistive pulse peaks, respectively. **(b)** SEM of a plastic-based XnCC consisting of an in-plane pore ($\mathbf{R}_{np}$), connecting extended nanochannels ($\mathbf{R}_{nc}$), and the microchannels ($\mathbf{R}_{mc}$). Each fluidic element is shown along with its respective fluidic resistance. (**c**) Equivalent sensing circuit for the XnCC, where $\mathbf{R}_{mc}$ is the resistance of the microchannel, $\mathbf{R}_{nc}$ is the resistance of extended nanochannel, $\mathbf{R}_{np}$ is the resistance of the in-plane pore, and $\mathbf{R}_{np}$ is the resistance of the particle. **(d)** Relevant equations for the measured signal ($\Delta\mathbf{I}$) measured from the open pore current ($\mathbf{I}_{open}$) and the in-plane pore occupied by a particle ($\mathbf{I}_{occupied}$). **(e)** Contour plot showing the relative current blockage signal that is generated for different particle sizes with respect to the pore size.

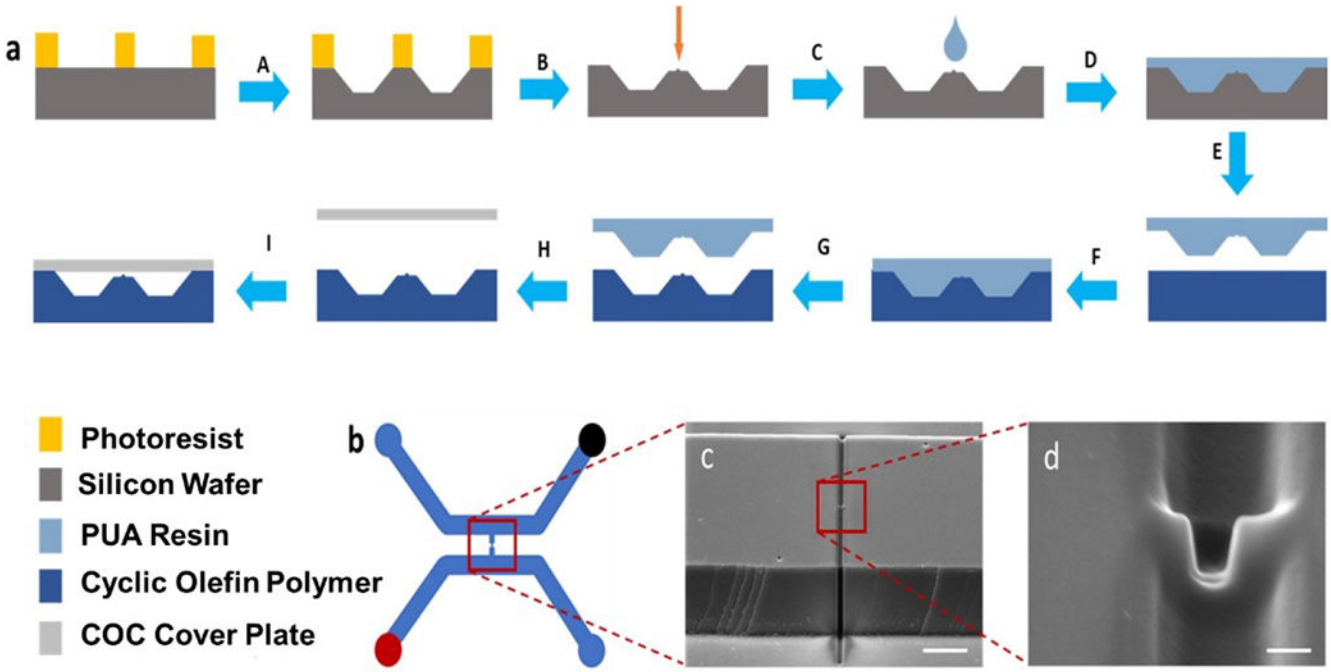

Fig. 2.

Fabrication steps of the fluidic circuit for the XnCC chip including the in-plane pore sensor. (**a**) Processing steps for creating the XnCC chip including: A) Photolithography followed by wet etching of the silicon wafer for generating microstructures; B) focused ion beam milling for producing the in-plane pore and connecting extended nanochannel; C) PUA resin stamp fabricated by UV-NIL; D) 185 nm exposure for 2.5 min to cross-link the PUA resin; E), F), and G) pattern transfer of the resin stamp pattern into COP using thermal NIL (conditions for the thermal NIL included 135°C and 2.07 MPa); H) and I) thermal fusion bonding between the imprinted COP substrate and COC cover plate (76°C and 0.83 MPa). (**b**) Schematic diagram of the XnCC chip (the colored reservoirs represent where the voltage was applied to the in-plane pore sensor. (**c**) SEMs of the XnCC master mold (scale bar = 5 μm). The cross-bridge channel (extended nanochannel) had a 500 nm width, 500 nm depth, and 15 μm length. (**d**) SEM of the in-plane pore sensor (scale bar = 200 nm). The pore has a 200 nm width, 200 nm depth, and 100 nm length.

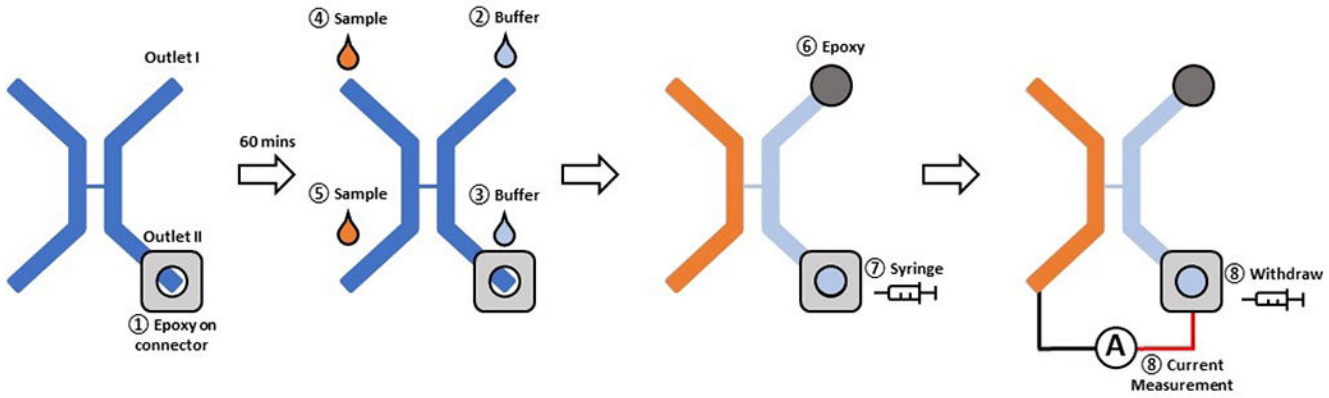

Fig. 3.

Operational steps associated with the XnCC chip. The withdrawal syringe connector was sealed to the assembled chip after fabrication (1). Buffer was then filled through one side of the XnCC chip (2, 3), and the sample was filled through the other side of the chip (3, 5). After solutions were successfully filled into the appropriate reservoirs of the XnCC chip, one of the buffer side reservoirs was sealed with epoxy (6), and the syringe pump was connected to the XnCC chip (7). The chip was then connected to the current amplifier for supplying the bias voltage and signal measurement (8).

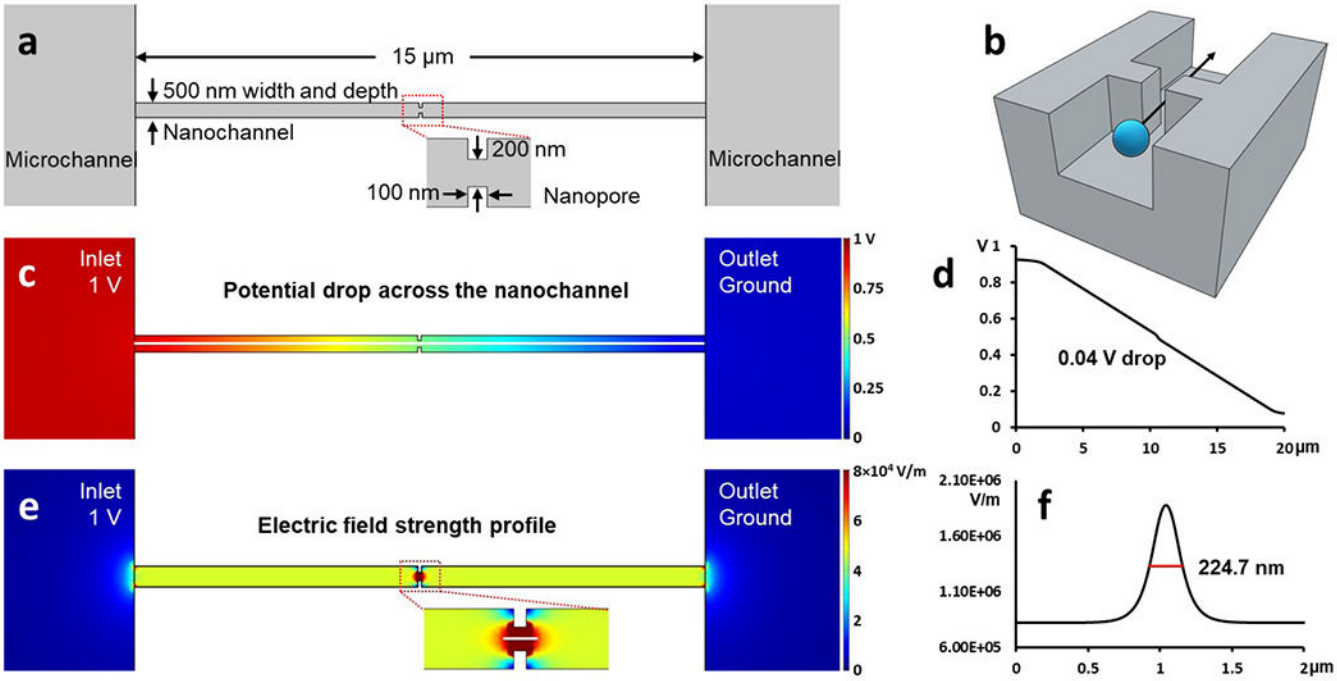

Fig. 4.

(**a**) 2D schematic of the connecting nanochannel with a length of 15 µm, 500 nm width, and 500 nm depth. The in-plane nanopore sensor had physical dimensions of 200 nm width, 200 nm depth, and 100 nm length. (**b**) 3D schematic of the connecting nanochannel with the in-plane nanopore sensor and a NP traveling through it. (**c**) Simulated voltage drop across the connecting nanochannel and inplane nanopore sensor. (**d**) Plot of potential drop vs. distance across the nanochannel and in-plane nanopore. The potential drop across the nanopore is 4% of the total field drop, but the length of the in-plane nanopore is only 0.7% of the total nanochannel length. (**e**) Simulated electric field strength profile in the microchannels, nanochannel, and nanopore. (**f**) The FWHM level of the full electric field strength was taken as the effective nanopore length, which was determined to be 224.7 nm from the simulation, but was designed to be 100 nm in the CAD drawing of the XnCC.

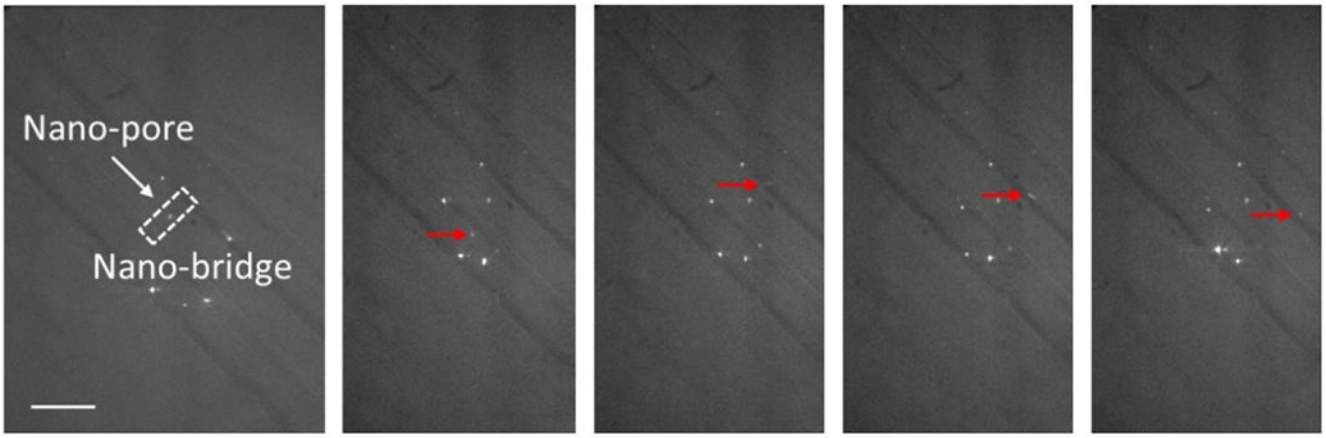

Fig. 5.

Still frames showing the movement of fluorescent polystyrene beads passing through the connecting nanochannel and nanopore. A single-molecule fluorescence tracking microscope was used herein (see Figure S1) that was equipped with a 63× objective and images were collected using a 100 ms exposure time. Scale bar = 20 μm. Red arrows are pointing to the location of a single bead.

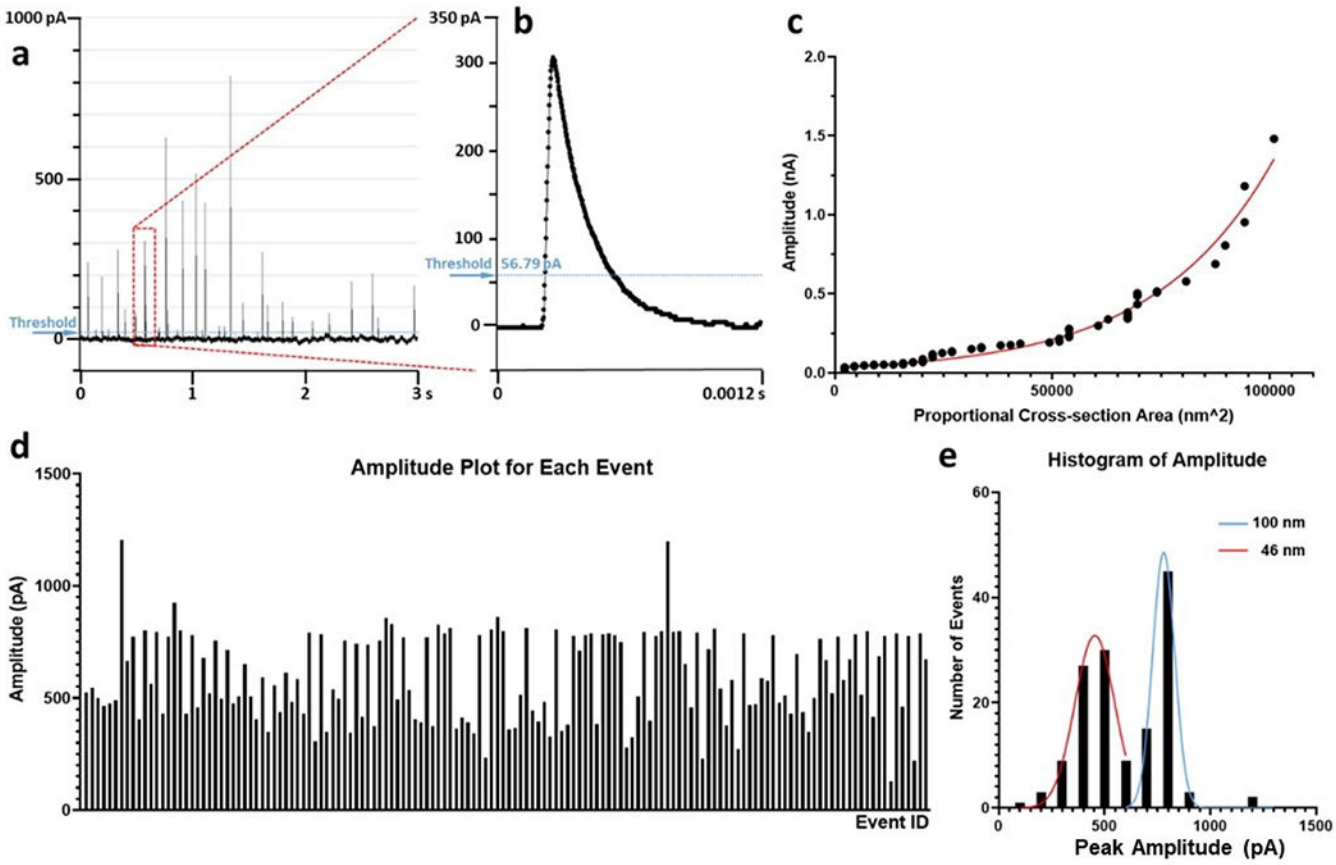

Fig. 6.

(**a**) Electrical signal trace generated from the nCC chip of the fluorescently-labeled polystyrene bead mixture (46 and 100 nm diameter). A threshold was set at 5× the standard deviation of a blank trace. The trace was analyzed by the pCLAMP software. (**b**) An expanded view of a single bead traveling through the nCC in-plane nanopore sensor, which gave a width of 0.9 ms and an amplitude of 308 pA. (**c**) Optical signals for a mixture of 46 and 100 nm beads and their correlation to nCC RPS signals, which was fit to a non-linear function with a correlation coefficient of $R^2 = 0.9991$ ($p < 0.0001$). (**d**) RPS amplitude plot for a mixture of 46 nm and 100 nm beads. (**e**) Histogram of the amplitudes of the XnCC peaks shown in (**d**). The histogram showed two normal distributions with two apparent means of 454 pA and 779 pA, which corresponded to the 46 and 100 nm beads, respectively.

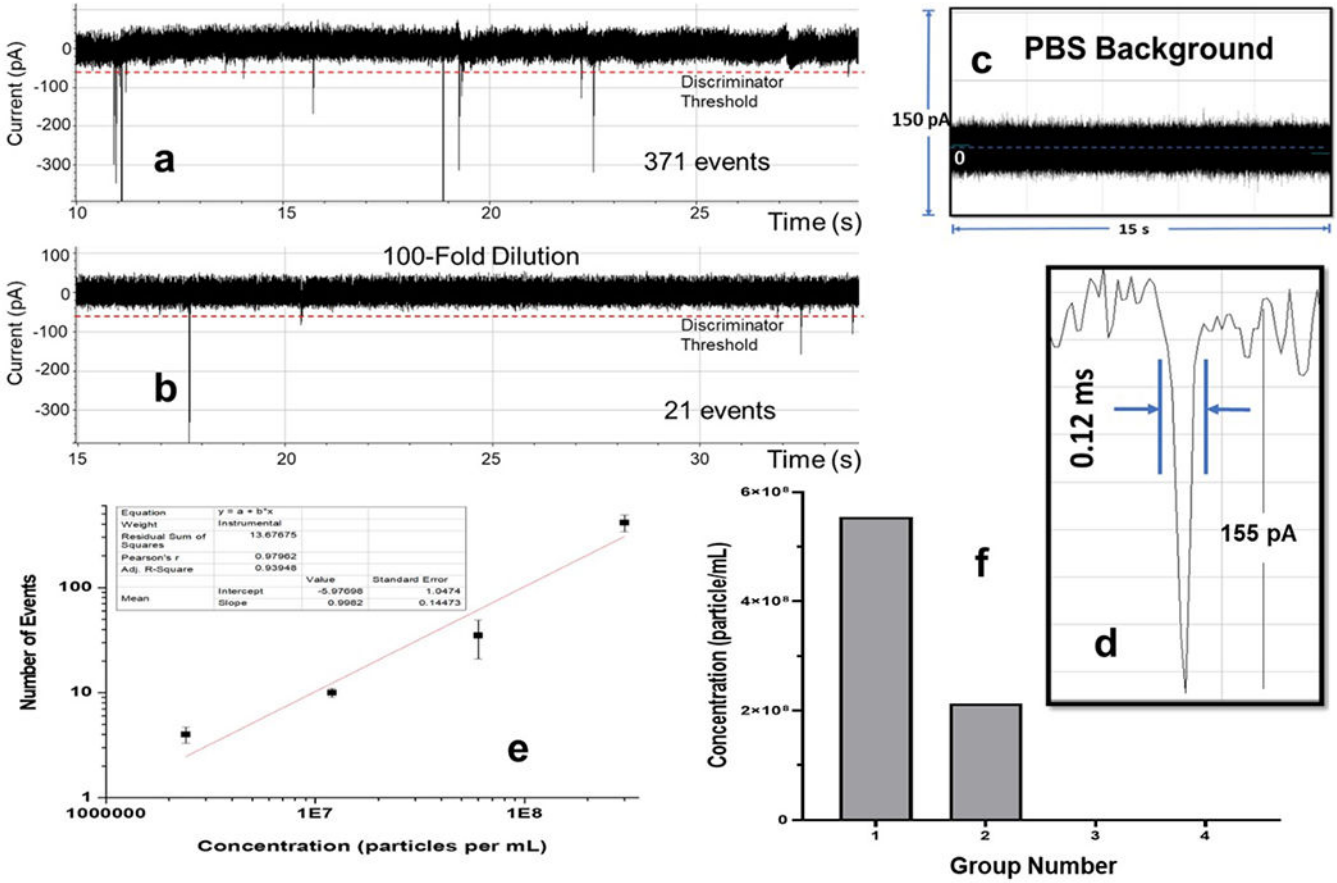

Fig. 7.

(a – b) RPS current traces of heat-inactivated SARS-CoV-2 VPs suspended in 1× PBS and traveling through the XnCC with a −1 V bias voltage. In (a), the concentration of VPs used here was ~5×10^8 VPs per mL, while in (b), the concentration in (a) was diluted 10-fold. The traces show data collected over 35 s, but the actual measurement time was 300 s. (c) Current trace data taken for a 1× PBS blank. (d) Expanded view of a single current transient peak taken from the trace in (a). (e) Standard curve of SARS-CoV-2 VP enumeration using the XnCC chip. These are heat-inactive VPs that were suspended in 1× PBS buffer. (f) Bar graphs for 4 saliva samples that were processed using the aptamer-selection chip, released from the capture surface of the chip, and enumerated by the XnCC chip. Samples 1 and 2 were loaded with SARS-CoV-2 particles at a level of 50/50 volume/volume of the stock solution and 1× PBS for Sample 1 and 25/50 volume/volume for Sample 2. Samples 3 and 4 were loaded with no SARS-CoV-2 particles. For the data shown in the calibration curve, a single device was used for each measurement. Therefore, the standard deviation represents the measurement and device variances.

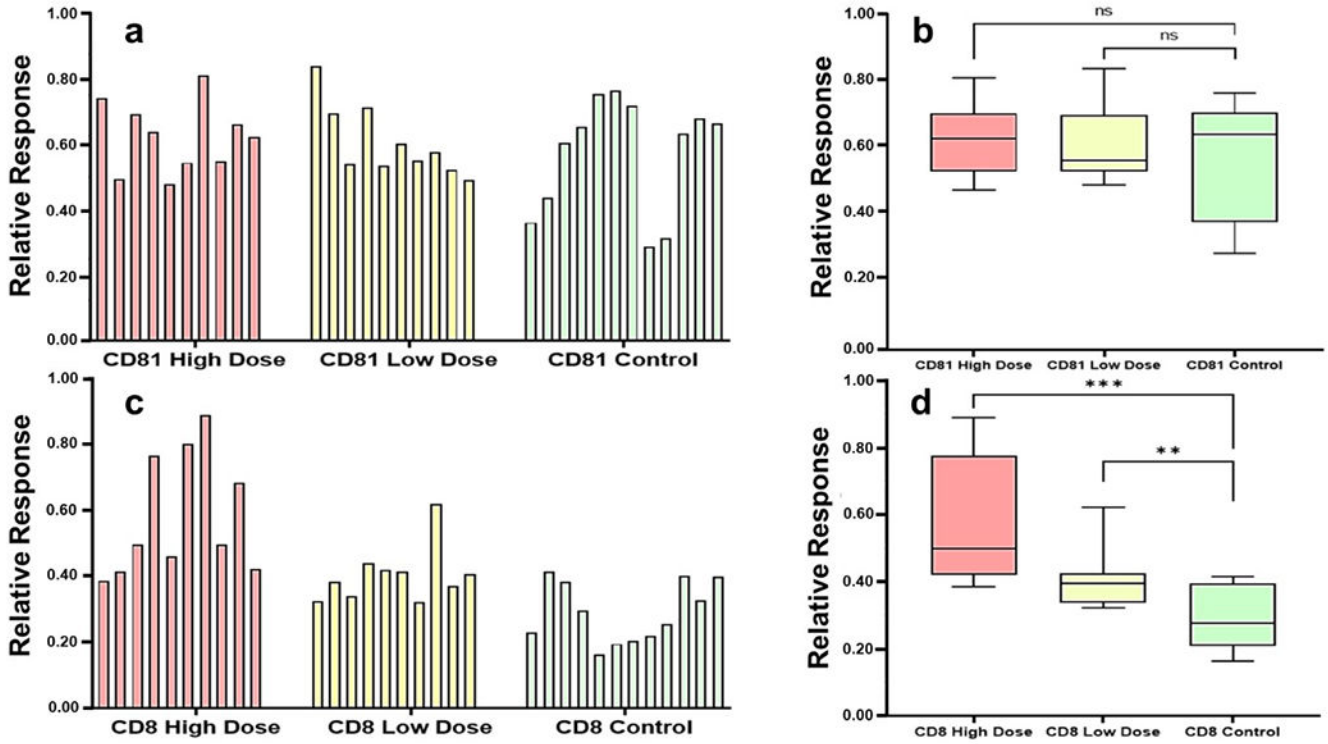

Fig. 8.

Mouse model plasma used for EV analysis for radiation exposure including 12 non-exposed mice (negative controls), 10 low dose radiation exposed mice (2 Gy), and 10 high dose radiation exposed mice (12 Gy) – positive controls. **(a)** Exosomes were isolated by anti-CD81 antibodies immobilized to the selection chip. **(b)** Among the three groups, there was no significant difference between the high dose, low dose or non-exposed groups. **(c)** EVs isolated using anti-CD8 antibodies immobilized to the selection chip. **(d)** Among the three groups, the amount of CD8 expressing EVs was statistically higher for the high dose group ($p = 0.0001$) and low dose group ($p = 0.0076$) compared to the non-exposed group. For these measurements, the BCA analysis was used. Each bar of the graph represents data from a single mouse model ($n = 10$) for the high dose, low dose, and control for both CD8 and CD81 selected EVs. The relative response for the y-axis represents particle concentrations for each sample normalized with respect to the highest concentration value (see CD8 high dose, sample #7).